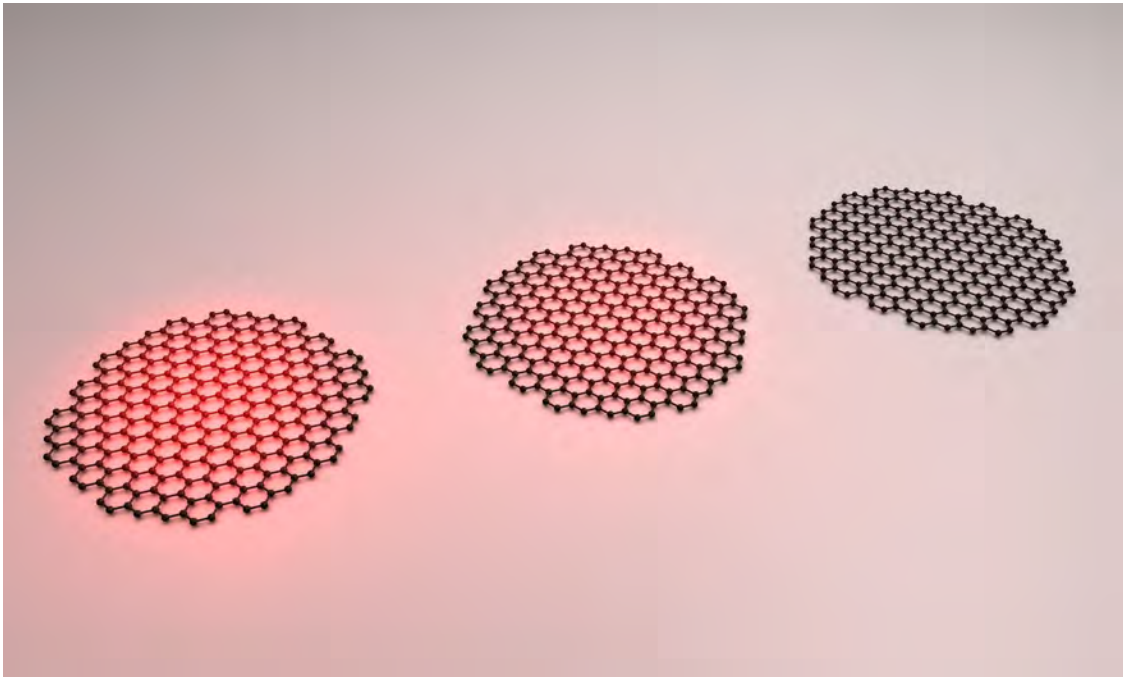


Temporal Evolution of Radiative Heat Transfer Between Graphene Nanodisks



Lauren Zundel

Work completed under the advisement of Prof. Alejandro Manjavacas

The University of New Mexico - May 7, 2019

Contents

Abstract	3
1 Introduction	5
1.1 Radiative Heat Transfer	5
1.2 Surface Plasmon Resonances	7
1.3 Graphene	8
2 Results	11
2.1 Description of the Model	11
2.2 Characterization of the Radiative Heat Transfer	14
2.3 Directional Heat Transfer	17
2.4 Creating an Alternating Pattern of Hot and Cold Disks	21
2.5 Isolating a Hot Disk	23
3 Conclusions	25
A Fluctuation-Dissipation Theorem	26
Acknowledgments	27

Abstract

In absence of conduction and convection, thermal equilibrium between objects and the surrounding environment is reached by means of radiative heat transfer, in which each object emits energy in the form of photons. The wavelength of this light is determined by the temperature and the optical properties of the object, and is, at the macroscale, accurately described using the Planck and Stefan-Boltzmann laws. When the dimensions of the objects, or the distances separating them, are reduced to below the so-called thermal wavelength, however, these laws break down; the unique interactions between light and structures smaller than or comparable in size to its wavelength can drastically alter this radiative heat transfer, allowing for rates far exceeding those predicted by these laws. Indeed, this behavior can be exploited as a mechanism to achieve new heat transfer scenarios that serve to advance a diverse range of technologies, including thermophotovoltaics and nanoscale circuits. One material that has exceptional promise to this end is graphene, a two-dimensional material composed of carbon atoms arranged in a honeycomb lattice; graphene can be electrically doped to support surface plasmons, the collective oscillations of the conduction electrons, at thermal wavelengths. Not only are the plasmons supported by graphene very strong and spectrally narrow, thus strengthening the interaction of graphene nanostructures with light of certain frequencies, the optical response of these structures can also be electrically tuned in real time, at rates limited by the speed of the electronics used. These properties enable a high level of active control over the absorption and emission, making graphene an ideal material for the manipulation of nanoscale energy transfer. In this work, we provide a comprehensive study of the temporal evolution of the radiative heat transfer in ensembles of graphene nanodisks. Specifically, we exploit the active tunability of graphene as a means to achieve new heat transfer scenarios that would not be possible with conventional, passive, materials. The results of this work serve to open new avenues for achieving complete control over nanoscale heat transfer by advancing the fundamental understanding of the dynamics of this process.

1 Introduction

The ability to manipulate the transfer of energy between objects poses a unique challenge that is of paramount importance for the advancement of a wide variety of new technologies that can revolutionize green energy [1], electronics [2], and space exploration [3]. From the ability to efficiently generate renewable energy to the thermal management of electronics, some of the most pressing issues of the modern day require complete dynamical control over the transfer of energy. In particular, as the ability to fabricate these technologies on a smaller scale grows, so too does the need for an increased level of control over the energy transfer that happens at the nanoscale. At this scale, the emergence of the unique interactions between light and matter constitute not only a unique challenge, but also an exciting opportunity to develop complete control over energy transfer. In this work, we describe a promising pathway to achieve fully dynamical control over nanoscale heat transfer based on the use of graphene nanostructures, whose strong optical responses can be actively tuned. Not only do our results serve to advance the fundamental understanding of energy transfer at the nanoscale, they will also serve as an inspiration for the development of a wide variety of improved technologies, including more efficient thermophotovoltaics, that can benefit from the new heat transfer scenarios we describe.

1.1 Radiative Heat Transfer

In absence of conduction and convection, the mechanism by which objects reach equilibrium with other objects and their environment is radiative heat transfer [4, 5]. In this process, energy is emitted in the form of light, at wavelengths determined by the temperature of the object. An idealized, extended system, which absorbs all light incident on it, is known as a blackbody. For a blackbody, the emission of light is described by the famous Stefan-Boltzmann law, which describes the temperature dependence of the overall emission, and Planck's law, which provides the wavelength dependence at a given temperature. In particular, for a blackbody, the power \mathcal{P} emitted per unit area A as a function of photon energy $\hbar\omega$ is given by

$$\frac{\mathcal{P}(\omega)}{A} = \frac{\hbar\omega^3}{3\pi^2c^2}n(\omega, T), \quad (1)$$

where $\hbar = h/2\pi$ is the reduced Planck's constant and c is the speed of light in vacuum. In addition, n is the Bose-Einstein distribution, defined as

$$n(\omega, T) = \frac{1}{e^{\frac{\hbar\omega}{k_B T}} - 1}, \quad (2)$$

where k_B is Boltzmann’s constant and T is the temperature. This equation describes emission in the far-field, *i.e.*, at distances much larger than the thermal wavelength $\lambda_T = 2\pi\hbar c/k_B T$. This wavelength, which ranges from approximately 7 mm at 2 K to 1.4 μm for 10^4 K, is on the order of 50 μm for a temperature of 300 K. Importantly, this equation describes the behavior of an extended structure, such as an infinite plane, that behaves as a blackbody.

When we have two blackbodies at different temperatures, they have a net transfer of energy between them from the hotter to the colder one. Since blackbodies absorb all light that is incident upon them, the heat transferred in the far-field limit, in which the distance separating the structures is larger than the thermal wavelength, is independent of this distance. This can be understood because the field of an extended structure is constant for distances much larger than the thermal wavelength.

On the other hand, when the separation between blackbodies is shrunk to a distance that is comparable to, or smaller than, the thermal wavelength, it is possible for extended structures to achieve rates of radiative heat transfer far exceeding this standard understanding. This is because, in this limit, the contributions from evanescent modes serve to augment the heat transferred between blackbodies [6–8]. In particular, the field has additional contributions that go as e^{-r} , r being the separation between structures. While this term is negligible for large r , it serves as a notable contribution to the emission in the near-field limit.

	 Extended Structures	 Finite Structures
Far-Field $r \gg \lambda_T$	$E = \text{Constant}$	$E \propto \frac{1}{r}$
Near-Field $r \ll \lambda_T$	$E \propto e^{-r}$	$E \propto \frac{1}{r^3}$

Table 1: Description of the near- and far-field behavior of extended and finite structures.

All of the discussion above applies to extended structures with infinite areas. However, when dealing with structures that are comparable in size to, or smaller than, the thermal wavelength, the situation is different. In particular, the far-field of a finite object decays as r^{-1} , rather than being constant, and the near-field goes as r^{-3} . This behavior, which is very different from that of extended structures, serves as an opportunity to achieve larger rates of radiative transfer than are achievable with extended blackbodies [9]. Table 1 shows a summary of the distance dependence of the electric fields produced by finite and infinite structures in the near- and far-field limits.

So far, we have only discussed the role played by the geometry of the system on the radiative transfer. However, the material properties can have an effect that is just as important. In particular, the presence of optical resonances can lead to absorption cross-sections that are much greater than

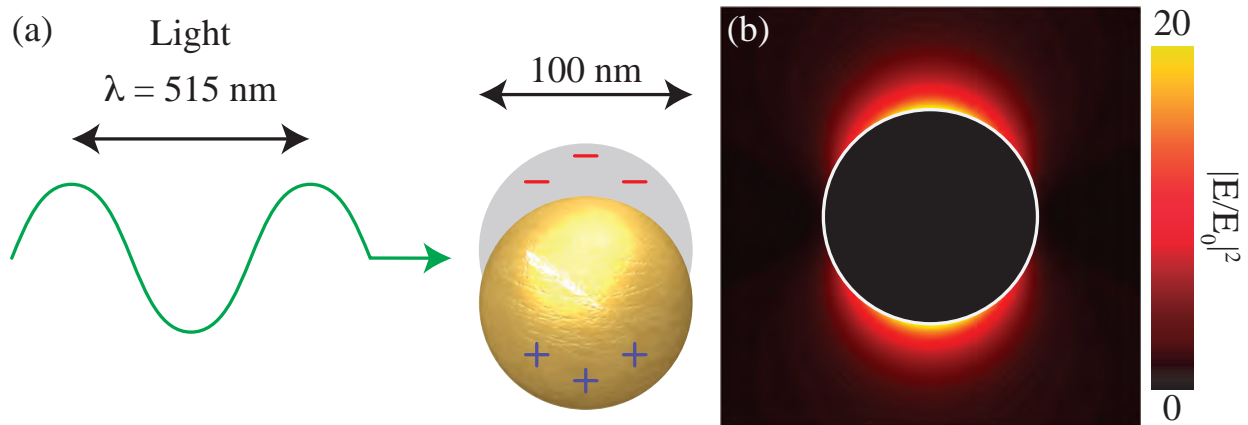


Figure 1: Surface plasmons in a gold nanosphere of radius $R = 50 \text{ nm}$. (a) Schematics showing the excitation of a surface plasmon using light with a wavelength of $\lambda = 515 \text{ nm}$. (b) Electric field intensity enhancement around the same gold nanosphere as in (a).

the area of the structure, and thus, radiative transfer that exceeds that of a blackbody having the same area [10]. In the following, we exploit all of this knowledge to manipulate the radiative heat transfer between nanostructures. In particular, we take advantage of the surface plasmon resonances supported by graphene nanodisks to achieve new heat transfer scenarios relying on active control.

1.2 Surface Plasmon Resonances

Surface plasmons are the collective oscillations of the free electrons in a metal [11], as depicted in panel (a) of Figure 1. When a metallic nanostructure is illuminated by light, the electrons in the structure will be displaced, which leads to a restoring force that serves to pull the electrons back to their original positions; the interplay between these forces, as dictated by the shape, size, and material properties of the nanostructure, results in the emergence of a resonance at a specific frequency of the light, which is known as the plasmon frequency.

One of the extraordinary properties of surface plasmons is that they interact strongly with light, enabling their application for such technologies as ultrasensitive biosensors [12, 13], vivid nanoscale color sources [14, 15], and efficient photovoltaic devices [16, 17]. This is because plasmons provide strong enhancement and confinement of the electromagnetic field in the subwavelength region surrounding a nanostructure [18, 19]. This can be seen in panel (b) of Figure 1, which shows the electric field intensity enhancement, $|E/E_0|^2$, surrounding a gold nanosphere of radius 50 nm at its plasmon frequency, $\lambda = 515 \text{ nm}$. The calculation shown was performed using the Boundary Element Method to solve Maxwell's equations by applying boundary conditions [20, 21], along with tabulated dielectric function data for gold that was taken from Reference [22]. We see

that, in a very small region around the surface of the nanosphere, the electric field intensity is on the order of 20 times that of the incident field. On the other hand, far from the plasmon resonance, the field enhancement will be negligible in comparison. This drastically altered behavior near the resonance frequency exemplifies the great promise of plasmonic nanostructures for manipulating near-field radiative heat transfer.

1.3 Graphene

One material that has, in recent years, emerged as an ideal tool to manipulate light below the diffraction limit is graphene [23,24]. Graphene is a two-dimensional monolayer of carbon atoms arranged in a honeycomb lattice, and has extraordinary optical properties. In particular, it can be doped with electrons by means of, for instance, electrostatic gating, thereby allowing it to support surface plasmons. The plasmons supported by graphene are exceptionally strong and spectrally narrow, and occur in the mid-infrared [25,26], which is the most relevant part of the spectrum for radiative heat transfer occurring under conventional temperatures. In addition, the frequency of the plasmons supported by graphene can be tuned by adjusting the doping level of the nanostructure [27,28]. This active tunability sets graphene apart from conventional plasmonic materials, whose size or shape must be adjusted to alter the optical response, and makes it an ideal material for use in a wide variety of applications where complete dynamical control is a necessity. For instance, graphene nanostructures are an ideal platform for use in Surface Enhanced Infrared Absorption (SEIRA) spectroscopy [29,30], a powerful tool for the detection of biological and chemical species in very low concentrations. This is achieved by exploiting the active tunability of graphene to align the position of the plasmon resonance with the natural vibrational modes of a molecule. Then, by placing molecules in the vicinity of the nanostructure, in areas with greatly enhanced fields, it is possible to amplify the optical signal of the molecule and thereby detect their presence.

The active tunability and strong plasmon resonances of graphene can also be applied as a mechanism to selectively absorb at specific frequencies, a principle that gives it great promise for use in manipulating radiative heat transfer. This is illustrated in Figure 2 (a), which shows the absorption cross-section per unit area of graphene nanodisks with different carrier concentrations. We characterize the carrier concentrations through their Fermi level, which corresponds to the energy of the electron in the highest occupied state, and is given by $E_F = \hbar v_F \sqrt{\pi |\rho|}$. Here, $v_F \approx c/300 \approx 10^6$ m/s is the Fermi velocity of electrons in graphene, and ρ is the electron density. The absolute value of this parameter is taken because the same behavior emerges when graphene is instead doped with holes. Using electrostatic gating, Fermi levels of up to 1.0 eV have been achieved [31].

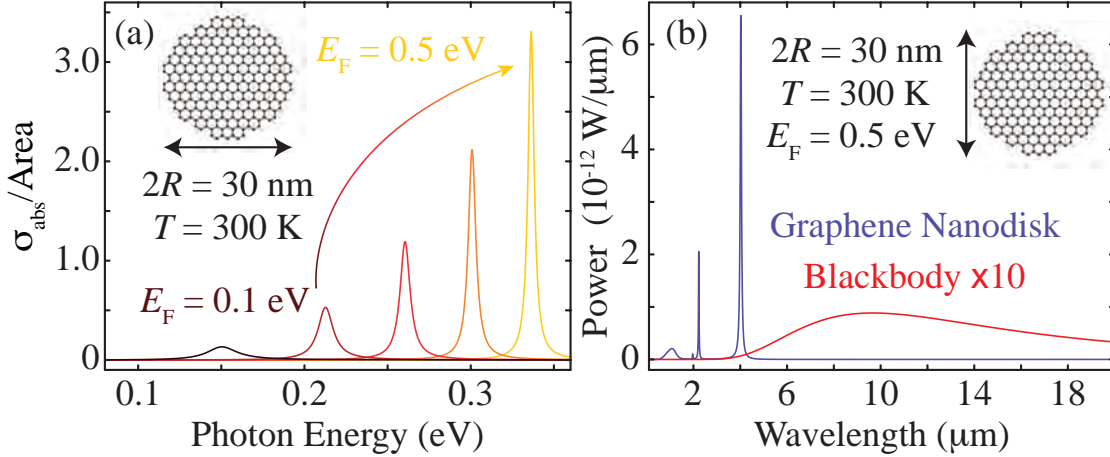


Figure 2: Tunability of graphene. (a) Absorption cross-section per unit area for a graphene nanodisk of radius $R = 15$ nm at $T = 300$ K with different Fermi levels E_F between 0.1 – 0.5 eV in steps of 0.1 eV, as represented by the colored curves. (b) Power emitted per unit wavelength for a graphene nanodisk with the same size and temperature as the one in (a) and Fermi level $E_F = 0.5$ eV (blue curve), compared to that of a blackbody at the same temperature and with the same area (red curve). The spectrum of the blackbody is multiplied by a factor of 10 for visibility.

In order to perform this calculation, we model the nanodisk as a point dipole, which is a valid approximation, given the drastic mismatch between the size of the nanodisk and the wavelength of light resonant with the plasmon. Within this approximation, the absorption cross-section is given by

$$\sigma_{\text{abs}} = 4\pi k \text{Im}\{\alpha\},$$

where α is the polarizability of the graphene nanodisk and $k = \omega/c = 2\pi/\lambda$ is the wavenumber. This mismatch between the size of the nanostructure and the wavelength of light also allows us to work in the electrostatic limit to describe the optical response of the nanodisk. In this limit, the in-plane polarizability of a graphene nanostructure can be modeled with the expression

$$\alpha(\omega) = \sum_i \frac{8R^3 \zeta_i^2}{(-1/\eta_i) - 2i\omega R/\sigma},$$

obtained using the plasmon wave function formalism (PWF) [31–33]. This expression allows us to describe the optical response of a nanostructure in terms of two parameters, η_i and ζ_i , whose values depend only on the shape of the nanostructure, and can be obtained by fitting the above equation to a rigorous solution of Maxwell’s equations. In this work, we take the sum over the first three dipolar modes. For a nanodisk, we have $\eta_1 = -0.0728$, $\zeta_1 = 0.8508$, $\eta_2 = -0.016$, $\zeta_2 = 0.4$, $\eta_3 = -0.0101$, and $\zeta_3 = 0.11$ [34]. In addition, the polarizability depends on the conductivity σ , which is a function of the temperature of the nanodisk, its Fermi level, and the electron mobility μ of the graphene. Here, we use a conductivity derived from the local limit of the random-phase

approximation for an extended graphene sheet [35], and, for all of the calculations described in this work, we assume an electron mobility $\mu = 3000 \text{ cm}^2/(\text{V s})$, a value that is well within current experimental capabilities [36] (note that values up to $10^5 \text{ cm}^2/(\text{V s})$ have been measured in h-BN encapsulated graphene samples [37, 38]).

Panel (a) of Figure 2 shows the absorption cross-section per unit area calculated using these tools for a nanodisk of radius $R = 15 \text{ nm}$ at a temperature $T = 300 \text{ K}$, as depicted in the inset. We perform these calculations for different Fermi levels in the range of $E_F = 0.1 \text{ eV}$ to 0.5 eV in increments of 0.1 eV , as indicated by the different colored curves. In particular, we see that the resonance frequency is shifted to a higher energy as the Fermi level is increased, and, additionally, the peak of the cross-section becomes significantly narrower and taller. The narrow nature of these resonances opens the door for systems in which one can adjust the doping level of graphene nanodisks in order to accurately select the frequency of light that will be absorbed.

The strong absorption cross-sections of doped graphene nanodisks also make it possible to achieve a higher level of control over the emission spectrum of these systems. Kirchoff's Law for thermal radiation tells us that the power emitted per unit frequency of an object is dictated by its absorption cross-section. In particular, the power emitted per unit area of a structure is [10]

$$\frac{\mathcal{P}(\omega)}{A} = \frac{\hbar\omega^3}{3\pi^2c^2} \frac{\sigma_{\text{abs}}}{A} n(\omega, T),$$

which, for a blackbody, reduces to Equation (1), since the absorption cross-section of a blackbody is always equal to its area. This also tells us that, when we have an absorption cross-section that is larger than the area of the nanostructure, as is the case near the plasmon frequency of graphene, we can achieve radiative heat transfer that is beyond that of an extended blackbody in the far-field. This is something that is only possible using finite objects, since, for infinite structures, the absorption cross-section per area will never exceed 1, but, for finite structures, it can. This can be seen in Figure 2, panel (b), where we show the power emitted per unit wavelength of a graphene nanodisk compared to that of a blackbody having the same finite area and temperature. In particular, as depicted in the inset of the panel, we consider a nanodisk of the same temperature ($T = 300 \text{ K}$) and dimensions ($R = 15 \text{ nm}$) as the one in panel (a), with a doping level of $E_F = 0.5 \text{ eV}$. The thermal emission spectrum of the graphene, plotted using the blue curve and characterized by its extraordinarily narrow spectral features, is significantly larger than that of a blackbody having the same temperature and area. Such a structure has a thermal emission given by Equation (1), and is plotted using a red curve. Indeed, the emission of the graphene nanodisk at certain frequencies is so much larger than that of the blackbody that the spectrum of the blackbody was multiplied by a factor of 10 in the plot for visibility, despite the fact that the area under the latter is larger overall. This exceptional increase in the emission around a very small frequency range makes graphene an

ideal tool to manipulate radiative heat transfer. Motivated by this, we study the radiative heat transfer between graphene nanodisks within an ensemble, with a particular focus on the time evolution of these systems. This inclusion of dynamics is a prospect that has hardly received any attention, despite some recent works discussing the radiative transfer between graphene nanodisks [39–41] and the great potential such a study has for application to new technologies.

2 Results

2.1 Description of the Model

We consider an arrangement of N point dipoles, each of which interacts with every other one in the system, as depicted in Figure 3. Because of the large mismatch between the wavelengths of light and the sizes of the structures we consider in this work, this dipolar approximation is valid for graphene nanodisks. Under this description, the power \mathcal{P} dissipated in a structure i within the ensemble is given by

$$\mathcal{P}_i = \left\langle \mathbf{E}_i(t) \cdot \frac{\partial \mathbf{p}_i(t)}{\partial t} \right\rangle, \quad (3)$$

where $\langle \rangle$ represents the average over thermal fluctuations, \mathbf{E}_i is the electric field of particle i , and \mathbf{p}_i is its dipole moment. For convenience, we choose to work in the frequency domain, defined via the Fourier transform,

$$\mathbf{p}_i(t) = \int_{-\infty}^{\infty} \frac{d\omega}{2\pi} \mathbf{p}_i(\omega) e^{-i\omega t}.$$

Then, Equation (3) becomes

$$\mathcal{P}_i = - \int_{-\infty}^{\infty} \frac{d\omega d\omega'}{(2\pi)^2} e^{-i(\omega-\omega')t} i\omega \langle \mathbf{E}_i^+(\omega') \mathbf{p}_i(\omega) \rangle, \quad (4)$$

where $^+$ indicates the conjugate transpose, and thus, in order to describe the radiative transfer, we only need to find the field and induced dipoles of each nanodisk. In order to do so, we make use of the coupled dipole model [42–45] to describe the response of each nanodisk. This model, whose use is justified here, due to the significant mismatch between the particle size and the wavelength of light, assumes that each nanodisk behaves as a point dipole that interacts with each other one in the ensemble, and is accurate when the center-to-center spacing of the

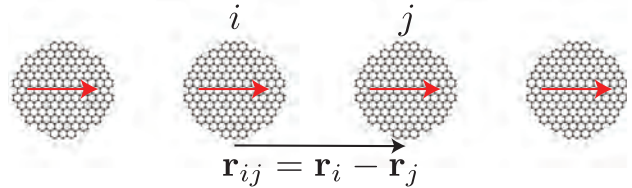


Figure 3: Sketch of the system under consideration, consisting of N interacting graphene nanodisks, which we model as point dipoles.

disks is at least three times the disk radius. Under this approximation, the induced dipole at disk i is given by

$$\mathbf{p}_i = \mathbf{p}_i^{\text{fl}} + \boldsymbol{\alpha}_i \mathbf{E}_i^{\text{fl}} + \alpha_i \sum_{j \neq i} \mathbf{G}_{ij} \mathbf{p}_j, \quad (5)$$

in terms of the sources, which are fluctuating dipoles \mathbf{p}_i^{fl} and fields \mathbf{E}_i^{fl} that result from the thermal motion of charges and currents in the system. Here, $\boldsymbol{\alpha}_i$ is a diagonal matrix with the three Cartesian components of the polarizability of dipole i (notice that the polarizability perpendicular to the disk is taken to be zero), and \mathbf{G}_{ij} is the dipole-dipole interaction tensor for dipoles i and j , which comes from the electric field of a unit dipole, and is defined for $i \neq j$ as

$$\mathbf{G}_{ij} = \frac{e^{ikr_{ij}}}{r_{ij}^3} [(kr_{ij})^2 + ikr_{ij} - 1] \mathcal{I}_{3 \times 3} - \frac{e^{ikr_{ij}}}{r_{ij}^3} [(kr_{ij})^2 + 3ikr_{ij} - 3] \frac{\mathbf{r}_{ij} \otimes \mathbf{r}_{ij}}{r_{ij}^2}, \quad (6)$$

and zero otherwise. Here, $\mathbf{r}_{ij} = \mathbf{r}_i - \mathbf{r}_j$ is the vector separating dipoles i and j , $r_{ij} = |\mathbf{r}_{ij}|$, and $\mathcal{I}_{3 \times 3}$ is the 3×3 identity matrix. In a similar fashion, we can write the electric field at each disk,

$$\mathbf{E}_i = \mathbf{E}_i^{\text{fl}} + \sum_{j \neq i} \mathbf{G}_{ij} \mathbf{p}_j + \mathbf{G}^0 \mathbf{p}_i, \quad (7)$$

where $\mathbf{G}^0 = (2/3)ik^3 \mathcal{I}_{3 \times 3}$ represents the radiation reaction term, which describes the emission of each dipole. Following the approach described in Reference [46], the solutions of Equations (5) and (7) can be written as

$$\mathbf{p} = \mathbf{A} \mathbf{p}^{\text{fl}} + \mathbf{B} \mathbf{E}^{\text{fl}} \quad (8)$$

and

$$\mathbf{E} = \mathbf{C} \mathbf{p}^{\text{fl}} + \mathbf{D} \mathbf{E}^{\text{fl}}, \quad (9)$$

where $\mathbf{A} = [\mathcal{I}_{3N \times 3N} - \boldsymbol{\alpha} \mathbf{G}]^{-1}$, $\mathbf{B} = \mathbf{A} \boldsymbol{\alpha}$, $\mathbf{C} = (\mathbf{G} + (2/3)ik^3 \mathcal{I}_{3N \times 3N}) \mathbf{A}$, and $\mathbf{D} = \mathcal{I}_{3N \times 3N} + \mathbf{C} \boldsymbol{\alpha}$, and the dipoles and fields now have $3N$ components, where N is the number of dipoles in the ensemble.

We use these expressions for the self-consistent dipoles and the field at each nanodisk in Equation (4). Since this equation requires an average of these values over thermal fluctuations, we apply the Fluctuation-Dissipation Theorem (see Appendix A), which is a relation derived in statistical physics that relates the fluctuations of a physical quantity with its dissipation. Using this tool, and after some lengthy algebra, we obtain the following result for the power dissipated in each disk:

$$\begin{aligned} \mathcal{P}_i &= \frac{2\hbar}{\pi} \int_0^\infty d\omega \omega \sum_j \text{Tr} [\text{Im}\{\mathbf{A}_{ij} \text{Im}\{\chi_j\} \mathbf{C}_{ij}^+\}] N_j \\ &\quad + \frac{2\hbar}{\pi} \int_0^\infty d\omega \omega \sum_{jj'} \text{Tr} [\text{Im}\{\mathbf{B}_{ij} \text{Im}\{G_{jj'}\} \mathbf{D}_{ij'}^+\}] N_0. \end{aligned}$$

Here, Tr indicates the trace over the Cartesian components, $N_i = n(\omega_i, T_i) + 1/2$, where $n(\omega, T)$ is the Bose-Einstein distribution, and T_i is the temperature of disk i . We reserve T_0 for the temperature of the environment. Furthermore, we use $\chi_i = \alpha_i(\omega) - (2i/3)k^3|\alpha_i(\omega)|^2$ to account for the radiative corrections and ensure that the optical theorem is satisfied for particles that are not absorbing [9]. By writing this result as

$$\mathcal{P}_i = F_i + \sum_{j \neq i} F_{ij} + \sum_{jj'} F_{i,jj'}^0,$$

we can understand it as the combination of the power lost by disk i with that which it has gained. In particular, F_i is the power lost to the environment and other disks, given by

$$F_i = \frac{2\hbar}{\pi} \int_0^\infty d\omega \omega \text{Tr} [\text{Im}\{\mathbf{A}_{ii} \text{Im}\{\chi_i\} \mathbf{C}_{ii}^+\}] N_i,$$

while F_{ij} is the power gained by disk i from disk j ,

$$F_{ij} = \frac{2\hbar}{\pi} \int_0^\infty d\omega \omega \text{Tr} [\text{Im}\{\mathbf{A}_{ij} \text{Im}\{\chi_j\} \mathbf{C}_{ij}^+\}] N_j.$$

Finally, $F_{i,jj'}^0$ is the power gained by disk i from the environment,

$$F_{i,jj'}^0 = \frac{2\hbar}{\pi} \int_0^\infty d\omega \omega \text{Tr} [\text{Im}\{\mathbf{B}_{ij} \text{Im}\{G_{jj'}\} \mathbf{D}_{ij'}^+\}] N_0.$$

It is convenient to define a heat transfer coefficient that is independent of the temperature. We can do this by linearizing the above equations with respect to temperature, and, for example, we find the expression for the heat transfer coefficient between the i^{th} and j^{th} disks of the ensemble to be

$$f_{ij} = -\frac{2\hbar}{\pi} \int_0^\infty d\omega \omega \text{Tr} [\text{Im}\{\mathbf{A}_{ij} \text{Im}\{\chi_j\} \mathbf{C}_{ij}^+\}] \frac{\partial n}{\partial T}.$$

Once we know the power absorbed by each nanodisk, we can compute the time evolution of

their temperatures by solving the differential equation

$$\frac{\partial T_i}{\partial t} = \frac{\mathcal{P}_i(T_0, T_1, \dots, T_N)}{C_{p,i}(T_i)}, \quad (10)$$

where, as described above, \mathcal{P}_i depends on the temperature of all of the objects in the ensemble, as well as that of the environment. In addition, $C_{p,i}$ is the heat capacity of graphene nanodisk i , calculated from the specific heat of graphene [47].

2.2 Characterization of the Radiative Heat Transfer

With the expressions for the heat transfer derived above, we can begin to work toward the main goal of this work, which is to study the time evolution of arrangements of graphene nanodisks that are exchanging heat. In order to do so, we first examine how the parameters of an ensemble of graphene nanodisks impact the heat transfer of the system without any time dependence. This allows us to determine the ideal electronic and geometric configurations for the fully dynamical control that we seek. The results of this characterization are shown in Figure 4. In particular, we consider a system of two graphene nanodisks of radius R and center-to-center separation a , the schematics of which are depicted in panel (a). Both of the disks are assumed to be at a temperature of 300 K, as is the environment. Although this equilibrium of temperatures between the two disks means that there will be no temperature change, and, thus, no net transfer, that does not mean that heat is not being exchanged between them. Rather, the fact that these two disks are at the same temperature as one another and the environment means that the total power emitted is the same as the total power absorbed for each disk.

The first parameters we study are the Fermi levels of the two disks, in an effort to determine the doping levels that will provide maximum and minimum radiative transfer. In particular, we consider disks of radius $R = 15$ nm and separation $a = 3R$. One of the disks has Fermi level E_{F1} , while the other is at E_{F2} . Panel (b) of Figure 4 shows the heat transfer coefficient f_{12} from Disk 1 to Disk 2 as a function of their Fermi levels. In particular, we note that f_{12} is maximized when the Fermi levels of the disks are equal, and decreases dramatically as the contrast between them is increased. The reason for this behavior is that, when there is a matching of the Fermi levels, the absorption and emission spectra of the disks will overlap the most, whereas, when there is a large contrast in the Fermi levels, they have very minimal overlap.

The Fermi level dependence also tells us that there is a finite Fermi level that gives us the optimal heat transfer between the disks. For the geometry considered here, we see that f_{12} is maximized in the interval $E_{F1} = E_{F2} = 0.08 - 0.22$ eV. The location of this maximum is determined

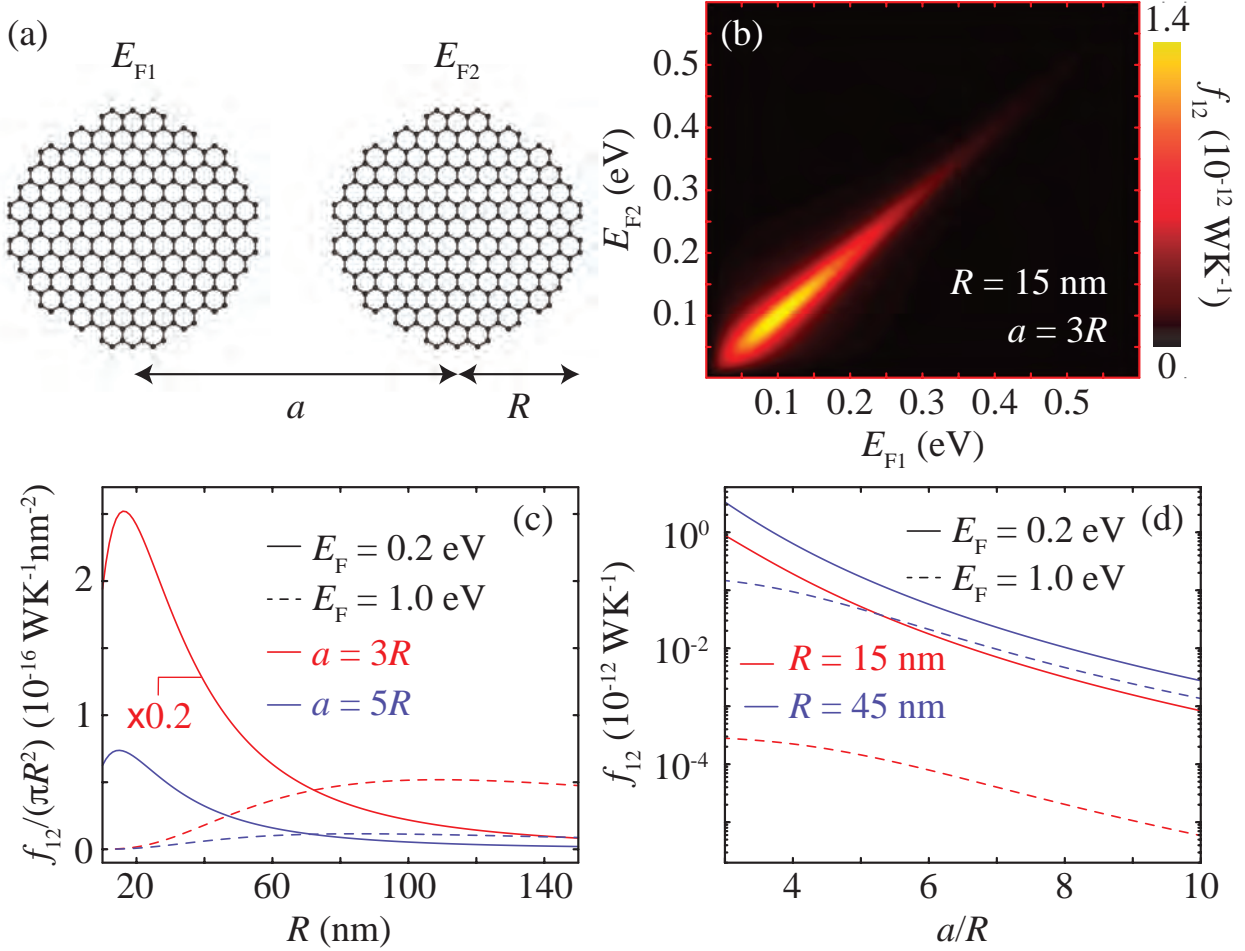


Figure 4: Heat transfer between two graphene nanodisks. (a) Schematics of the system under consideration, composed of two graphene nanodisks of equal radius R and center-to-center separation a . Both nanodisks are held around a temperature of $T = 300$ K, as is the environment. The left disk has Fermi level E_{F1} , while the right disk is at E_{F2} . (b) Plot of the heat transfer coefficient f_{12} from Disk 1 to Disk 2 at $T = 300$ K as a function of E_{F1} and E_{F2} for $R = 15$ nm and $a = 3R$. (c) Heat transfer coefficient f_{12} per disk area πR^2 from Disk 1 to Disk 2 as a function of R . The red curves correspond to $a = 3R$, whereas the blue ones represent $a = 5R$. The solid and dashed curves, respectively, represent $E_{F1} = E_{F2} = 0.2$ eV and $E_{F1} = E_{F2} = 1.0$ eV. Note that, for visibility, the curve corresponding to $a = 3R$, $E_F = 0.2$ eV is multiplied by a factor of 0.2. (d) Heat transfer coefficient f_{12} at $T = 300$ K from Disk 1 to Disk 2 as a function of a/R . The red and blue curves show results for $R = 15$ nm and $R = 45$ nm, respectively, while the solid and dashed curves represent $E_{F1} = E_{F2} = 0.2$ eV and $E_{F1} = E_{F2} = 1.0$ eV.

based on the interplay between the polarizabilities of the nanodisks and the Bose-Einstein distribution from Equation (2). As the Fermi level of each disk is increased, it will have a stronger response, and thus a stronger interaction with other disks in its vicinity. However, the resonances are also shifted to a higher energy with this increase in Fermi level. Since the heat transfer between the disks is also dependent on the Bose-Einstein distribution, which decreases drastically with increasing energy, the optimal Fermi level for heat transfer relies on a balance between these two factors. We are focusing, in this work, on temperatures between 200 K and 400 K, so, in the following, we analyze a Fermi level of 0.2 eV, which will be the optimum for emission at the highest temperature.

The polarizability of the graphene nanodisks also depends on their size, so we next investigate the dependence of the heat transfer coefficient on the radius of the disks. In panel (c), we plot the heat transfer coefficient per unit area, $f_{12}/(\pi R^2)$, as a function of the radius R for four different combinations of geometries and doping scenarios. For this plot, we assume the size of both of the disks, as well as their Fermi levels, to be equal, and we investigate cases corresponding to both high and low levels of radiative transfer from panel (b). Specifically, the solid curves correspond to Fermi levels of 0.2 eV, with the red one depicting the results for a separation of $a = 3R$, and the blue one representing $a = 5R$. On the other hand, the dashed curves with the same colors correspond to the heat transfer between disks having the same separations as before, but when the Fermi level is 1.0 eV instead. We note that there is an optimum radius for heat transfer, which depends on the separation between the nanostructures, as well as their Fermi levels. In addition, we find that the heat transfer is significantly greater when the disks are much closer together. This result is completely expected, since the strength of the interaction between the disks is heavily dependent on the distance separating them, as shown in Equation (6).

In order to confirm this, we next study the dependence of f_{12} on the distance separating the two disks. In panel (d), we show four configurations, corresponding to different combinations of size and doping level of the disks. As in panel (c), the dashed curves correspond to a Fermi level of 1.0 eV, whereas the solid curves represent the case where this quantity is 0.2 eV. The red and blue curves, respectively, show the results for disks of radius 15 nm and 45 nm. As expected, the heat transfer coefficient rapidly drops with increasing separation.

The results shown in this figure provide the foundation for the rest of this work, since they serve to inform our choice of parameters for the doping levels and geometry of the systems we consider. Through a careful choice of the Fermi levels of each disk within an ensemble, we can couple certain disks while minimizing the interaction with others; this opens up the door to achieving new, exotic heat transfer scenarios that would be difficult, if not impossible, to achieve without the strong response and active tunability of graphene. In the following, we investigate several such examples.

2.3 Directional Heat Transfer

The first example of a tunable heat transfer scenario we investigate is the possibility to send heat in a desired direction. As described in the previous section, by tuning the electric properties of each nanodisk within an ensemble, it is possible to maximize the interaction between certain disks, while minimizing the heat transfer to and from others. In the time domain, this translates to disks with the same Fermi levels exhibiting much faster thermalization than those with drastically different ones. As a preliminary case, we consider a system of two graphene nanodisks of equal size $R = 15$ nm and center-to-center separation $a = 3R$, as depicted in panel (a) of Figure 5. One of the disks (red) has a constant Fermi level $E_{F1} = 0.2$ eV and begins at a temperature of 400 K. On the other hand, the doping level of the other disk (blue), which begins at 200 K, is chosen to either maximize ($E_{F2} = 0.2$ eV, dashed curves) or minimize ($E_{F2} = 1.0$ eV, solid curves) the radiative transfer between the two disks. Given these two scenarios, we find the time dynamics, shown in panel (a) in colored curves matching the respective disks, using the fourth order Runge-Kutta method to solve Equation (10). As expected from our results in the previous section, the radiative transfer between the disks is maximized when the Fermi levels are equal (at a value of $E_F = 0.2$ eV). This allows the nanodisks to thermalize in roughly $1 \mu\text{s}$. On the other hand, when there is a high contrast in the Fermi levels of the disks, their temperatures remain almost entirely unchanged over ten times as long. This is because the time it takes for the disks to thermalize is a direct result of the value of the heat transfer coefficient between the disks, which is minimized for Fermi levels that have large contrast, and maximized when the Fermi levels overlap.

This profound difference in behaviors under the two doping scenarios shows extraordinary promise to be applied to much more complicated systems as a way to achieve complete control over which disks can thermalize with one another and the time scales over which they can do so. Specifically, this principle can be applied as a way to direct energy along one direction, with minimal impact on other disks. We show a simple example of this in panel (b), in which we have a chain of three nanodisks, as depicted in the schematics above the plot. All of the disks have uniform size $R = 15$ nm and center-to-center separation $a = 3R$. The central disk (red, denoted Disk 2) has Fermi level $E_F = 0.2$ eV and begins at 400 K. The disks on either side of it, however, begin at 200 K and have different Fermi levels. The leftmost one (green, Disk 1) has a doping level chosen so that it shares maximal heat transfer with the central disk (*i.e.*, $E_F = 0.2$ eV). On the other hand, the rightmost disk (blue, Disk 3) has a Fermi level $E_F = 1.0$ eV, chosen so that it will accept minimal heat from the other disks. The temporal evolution of the temperature of each disk, again plotted in colors that correspond to the color of its respective disk within the schematics, shows that the heat is almost solely transferred from Disk 2 to Disk 1; these disks thermalize with one another in roughly $1 \mu\text{s}$ and leave the third disk almost exactly at its starting temperature, even

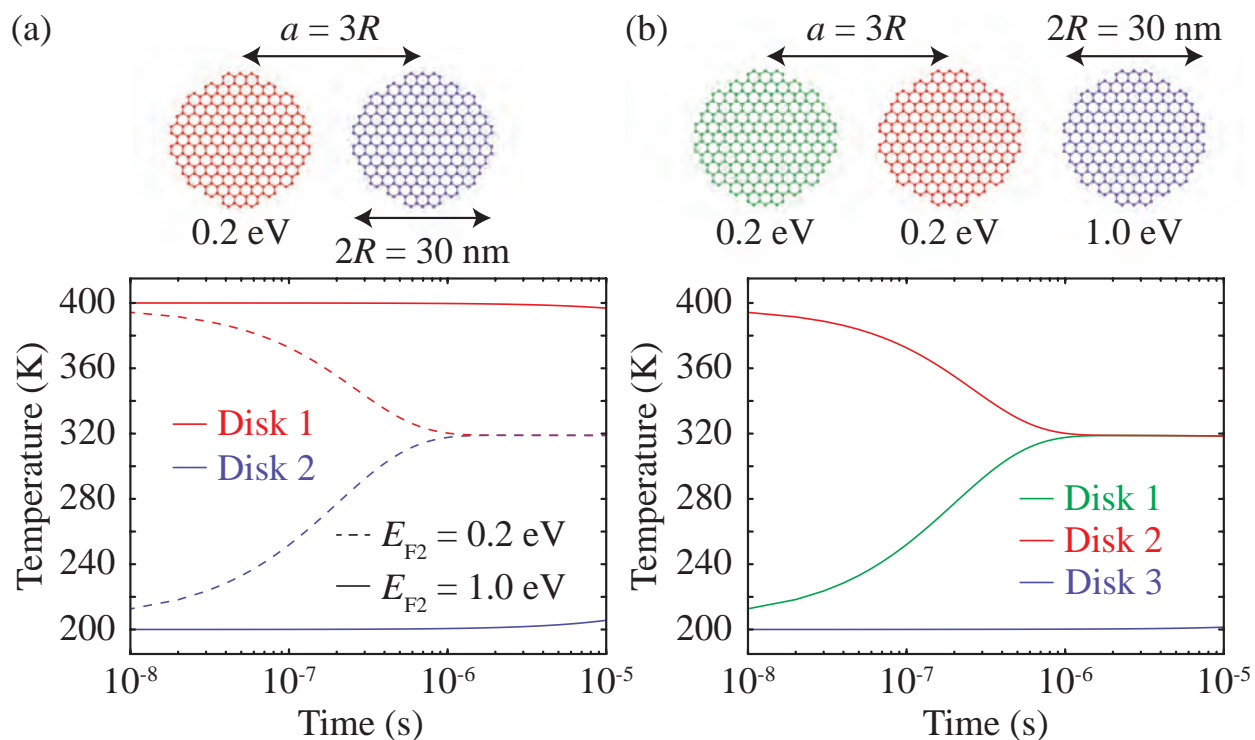


Figure 5: Time evolution of radiative heat transfer between two and three graphene nanodisks. (a) Heat transfer between two graphene nanodisks of radius $R = 15$ nm and center-to-center separation $a = 3R$, as depicted in the upper schematics. One disk (red) begins at $T = 400$ K with constant Fermi level $E_{F1} = 0.2$ eV, while the other disk (blue) begins at $T = 200$ K and has Fermi level $E_{F2} = 0.2$ eV (dashed curves) or $E_{F2} = 1.0$ eV (solid curves). The environment is held at $T = 300$ K. (b) Radiative heat transfer between three graphene nanodisks with the same sizes and separation as in (a) and depicted in the schematics. The central disk (red) begins at $T = 400$ K, whereas the other two disks (green and blue) begin at $T = 200$ K. The central disk, as well as one of the edge disks (red and green, respectively) have Fermi levels $E_{F1} = E_{F2} = 0.2$ eV, while the other disk (blue) is at $E_{F3} = 1.0$ eV. As in (a), the environment has temperature $T = 300$ K.

after $10 \mu\text{s}$.

The concept demonstrated in Figure 5 can, in principle, be applied to a chain containing an arbitrary number of disks. For example, in Figure 6, we examine the dynamics of a chain of 7 nanodisks, all of which begin at temperature 200 K and have Fermi level $E_F = 0.2 \text{ eV}$. As indicated by the schematics, shown in panel (a), we place an additional disk that acts as a heat source (red) on the left-hand side of the chain, and one that is a heat sink (blue) on the other side. The heat source is held at a constant temperature of 400 K, and the heat sink is maintained at 200 K. By modulating the Fermi levels of these two disks, thereby connecting or disconnecting them from the rest of the chain, we can thus send heat back and forth along the chain. Panel (b) shows the Fermi levels of the heat sink and source as a function of time; the heat source begins at $E_F = 0.2 \text{ eV}$, thus connecting it to the chain, while the heat sink is at $E_F = 1.0 \text{ eV}$ to minimize its interaction with the rest of the system. At a time $t = 30 \mu\text{s}$, the Fermi levels of the source and sink are flipped, so that the chain will interact instead with the heat sink and thus be cooled back down.

Panel (c) of Figure 6 shows the time evolution of the temperature of each disk within the chain for a single heating and cooling cycle. The colored lines correspond to the temperatures of the disk labeled using the same color in panel (a). At the beginning, over a period of $30 \mu\text{s}$, the heat quickly propagates through the chain, with the first disk thermalizing in approximately $20 \mu\text{s}$, and the rest following sequentially afterward. This cascading effect comes as a result of the distance dependence on the heat transfer. As discussed in Figure 4, the heat transfer drastically drops off as the separation between the disks is increased, so it is unsurprising that the heat exchanged between the farthest disks and the sources or sinks will take much more time to have an impact on the temperature.

When the Fermi levels of the heat sink and source are switched, so that the disks now primarily interact with the heat sink, the disks, as expected, cool down to their original temperatures. As was the case with the heating phase of these results, the heat propagates through the chain, this time toward the heat sink. That is to say that the disks closer to the sink thermalize with it more quickly, while the further ones follow close behind. This thermalization with the heat sink restores the disks to their beginning state, completely reversing the effects of the heating phase on the chain. Therefore, once the disks return to their starting temperature, they can be recoupled to the heat source, and subsequently the heat sink, thus repeating the entire process over again. This reversibility, combined with the ability to direct heat through a chain, is a powerful tool to achieve complete temporal control over radiative transfer.

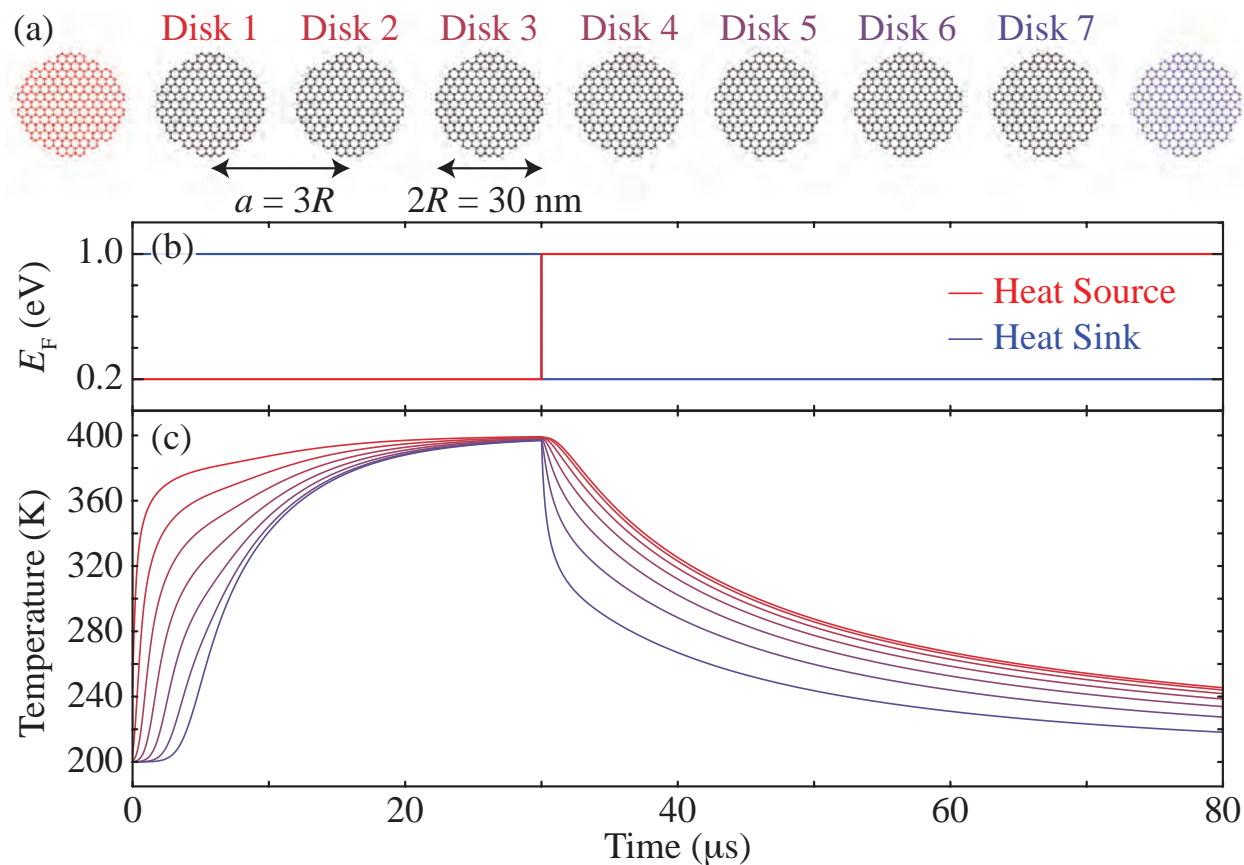


Figure 6: Directional heat transfer. (a) Schematics of the system under consideration, consisting of 7 graphene nanodisks of radius $R = 15$ nm and center-to-center separation $a = 3R$. On the left-hand side of this chain, a heat source (red disk) is held at a constant temperature 400 K, and, placed on the right-hand side is a heat sink (blue disk) at a constant 200 K. All of the disks in the chain, except for the heat source and heat sink, are held at a constant Fermi level of 0.2 eV. (b) Plot of the Fermi level of the heat source (red curve) and heat sink (blue curve) as a function of time. (c) Temperature of the nanodisks in the chain as a function of time. The color of each curve is chosen to correspond to the color of the label above its respective disk in panel (a).

2.4 Creating an Alternating Pattern of Hot and Cold Disks

We can also apply the knowledge gained from our characterization of the system to achieve other exotic heat transfer scenarios. For instance, by carefully choosing which disks within an ensemble will be thermally connected to a heat source or heat sink, we can create specific distributions of heat that can be maintained for long periods of time.

Here, we investigate this prospect to develop an alternating pattern of hot and cold nanodisks. In order to do this, we consider a setup like the one shown in panel (a) of Figure 7. This setup consists of two parallel chains of 5 nanodisks having radius $R = 15$ nm and center-to-center separation $a = 3R$. On the left-hand side of the lower chain, there is a heat source of constant temperature 400 K, which is colored red in the schematics, whereas, on the right-hand side, there is a heat sink held at 200 K that is colored blue in the figure. By carefully choosing the Fermi levels of the disks within the chain, as well as those of the source and sink, we can heat up a specific pattern of disks from the upper chain, while keeping the rest of the disks in that chain cool. We achieve this using the coupling scenario described in panel (b), which displays the Fermi levels of the heat source and sink, with curve colors corresponding to the color of the disk it represents in (a), and panel (c), which shows the Fermi levels of the upper chain of disks, as indicated by the legend. The lower chain of the disks is always 0.2 eV. We create an alternating pattern of hot and cold disks by connecting the entire lower chain, and the disks chosen to be heated, by setting their Fermi level equal to that of the heat source. For this purpose, we choose a Fermi level of $E_F = 0.2$ eV, as discussed previously, because this value gives a strong interaction between the disks, thereby making the thermalization process very rapid. All of the other disks, as well as the heat sink, are held at $E_F = 1.0$ eV, with the goal of minimizing the heat that they draw from the heat source and disks that are being heated.

The time dynamics of the temperatures of the disks in the top chain are shown in panel (d), with color of each curve corresponding to the color of the label above the disk it represents in panel (a). After a period of $20 \mu\text{s}$, the heated disks are thermalized with the heat source, creating an alternating pattern among the top chain. In order to demonstrate that this system allows us to create completely arbitrary patterns of hot and cold disks, we then cool all of the disks back to their original temperature, thereby restoring the system to its initial state. We achieve this by setting the Fermi level of the heated disks, as well as that of the heat sink, to $E_F = 0.2$ eV at a time $t = 20 \mu\text{s}$, while the heat source and cool disks are changed to $E_F = 1.0$ eV. As expected, this maximizes the interaction of all of the heated disks with the heat sink, while minimizing interactions with the heat source, allowing the disks to cool.

At a time $t = 80 \mu\text{s}$, we then change the Fermi levels of the system in order to heat up a new pattern of disks along the upper chain. Specifically, we choose an alternating pattern in which

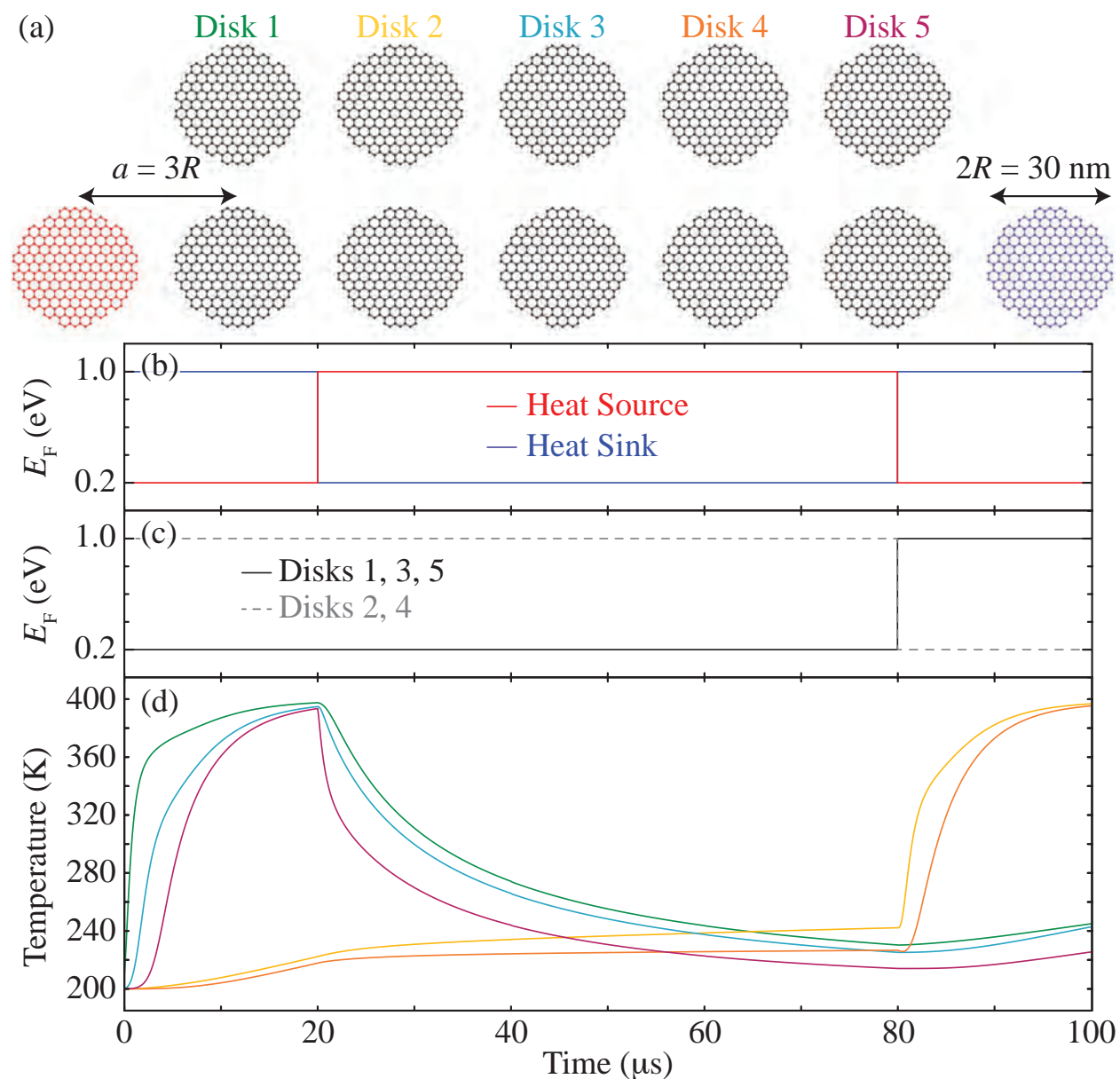


Figure 7: Creating an arbitrary pattern of hot and cold nanodisks. (a) Schematics of the system under consideration, consisting of two chains of 5 nanodisks of radius $R = 15 \text{ nm}$ and center-to-center separation $a = 3R$. On the left-hand side of the bottom chain, there is a heat source (red) of constant temperature 400 K, while, on the right-hand side, there is a heat sink (blue) held at 200 K. The disks in the chains begin at a temperature 200 K, and the environment is assumed to be 300 K. (b) Plot of the Fermi levels of the heat source and sink, with curves in the respective colors of the disks from (a). (c) Plot of the Fermi level of the disks in the upper chain. The gray dashed curve correspond to that of Disks 2 and 4 in panel (a), while the black solid one is for Disks 1, 3, and 5. The Fermi level of all of the disks in the bottom chain is held constant at 0.2 eV. (d) Plot of the time dynamics of the temperature of each disk in the top chain. Each curve is given a color that corresponds to the label above its respective disk in panel (a).

the new heated disks are those that were kept cool during the first heating period. To this end, those disks, as well as the ones in the lower chain, and the heat source, are assigned a Fermi level $E_F = 0.2 \text{ eV}$, while every other disk, including the heat sink, is at $E_F = 1.0 \text{ eV}$. After a period of about $20 \mu\text{s}$, the desired disks are thermalized with the heat source, while the adjacent disks remain cool; once again, an alternating pattern has been developed in the upper chain of nanodisks, demonstrating the high level of control we have over the heat transfer throughout the ensemble.

2.5 Isolating a Hot Disk

Another arrangement we consider is one that will allow us to heat a nanodisk and leave it isolated by cooling its neighbors. In principle, this should allow us to store energy in the isolated disk for long periods of time before releasing it at the desired moment. In order to demonstrate this prospect, we consider a chain of 5 nanodisks, as the one shown in Figure 8 (a). Each nanodisk has a radius $R = 15 \text{ nm}$ and center-to-center separation $a = 3R$. The chain is surrounded on either side by both a heat sink (blue), held at a temperature $T = 200 \text{ K}$, and a heat source (red), held at $T = 400 \text{ K}$. All of the disks in the chain begin at a temperature $T = 200 \text{ K}$, while the environment is at $T = 300 \text{ K}$.

We first want to heat up the chain of disks to 400 K . In order to do so, we set their Fermi levels, as well as those of the heat sources, to $E_F = 0.2 \text{ eV}$. On the other hand, the heat sinks are at $E_F = 1.0 \text{ eV}$, so that their interaction with the other disks is minimal. Once the disks are thermalized with the heat source, at a time $t = 5 \mu\text{s}$, we switch the Fermi level of the central disk in the chain, as well as the heat sources, to $E_F = 1.0 \text{ eV}$, while the heat sinks are changed to $E_F = 0.2 \text{ eV}$. This is shown in panel (b), where we plot the Fermi levels of the heat sources (red curves) and sinks (blue curves) as a function of time, as well as (c), where we do the same for the central disk. During the entire process, the other disks within the chain stay at $E_F = 0.2 \text{ eV}$. This is so that we can cool the chain, except for the central disk, back to the starting temperature. The central disk thus remains hot, despite all of the adjacent disks being cold. We show this in panel (d), with each colored curve corresponding to the time evolution of the temperature of the disks within the chain that are labeled using the same color in panel (a). Note that, because of the symmetry of our ensemble, the temperatures of the disks surrounding the central one are the same to the left and the right; we therefore label these disks with the same colors.

During the heating portion of the calculation, the disks rapidly thermalize with the heat source. When the coupling is changed, so that the chain can cool, the disks more slowly thermalize to the heat sinks. This asymmetry is a result of the different conductivity of the nanodisks at different temperatures, which alters the optical response, and therefore the temporal evolution.

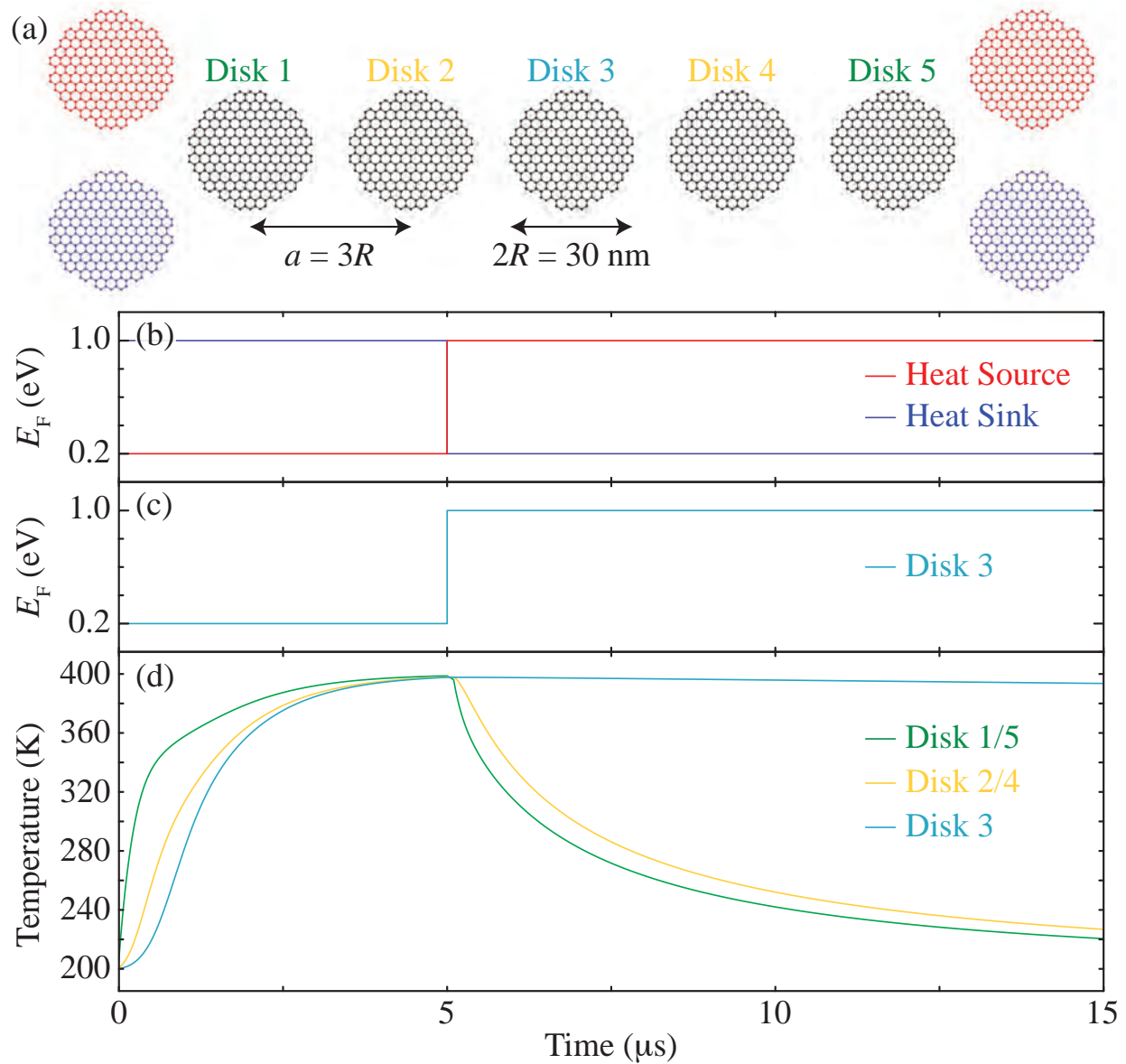


Figure 8: Isolation of a hot nanodisk. (a) Schematics of the system under consideration, consisting of 5 graphene nanodisks in a chain and two additional nanodisks, one of which is a heat sink (blue disks) held at constant temperature $T = 200 \text{ K}$, and the other being a heat source (red disks) held at $T = 400 \text{ K}$, on either side of the chain. All of the nanodisks have $R = 15 \text{ nm}$, and the separation between each disk is $a = 3R$. (b) Plot of the Fermi levels of the heat source (red curve) and heat sink (blue curve) disks as a function of time. (c) Plot of the Fermi level of Disk 3, which is the only one in the chain whose Fermi level is not held constant at $E_F = 0.2 \text{ eV}$. (d) Plot of the temperature evolution of the disks in the chain as a function of time. The color of the curves corresponds to the disk with the same colored label in (a). Because the system is symmetric, Disks 1 and 5 (green), as well as 2 and 4 (yellow), have the same temperature.

However, we also note that, in the period of time that it takes for the disks to cool back down to 200 K (approximately $10 \mu\text{s}$), the central disk barely changes from its higher temperature. Although, over much longer time scales, the disk would inevitably cool down, since it remains out of equilibrium for as long as its temperature is different from its surroundings, the drastically different Fermi levels, and thus emission and absorption peaks of the disk and its neighbors, serves to mostly keep this disk thermally isolated. This implies that the energy in the disk can be stored and released at will, and is minimally impacted by its surroundings when they have highly contrasting Fermi levels. The ability to isolate a hot disk in this way shows the great promise for these systems to be exploited for thermal management and evidences the high level of control over heat transfer that can be achieved using graphene.

3 Conclusions

In conclusion, we have performed a comprehensive analysis of the temporal evolution of the radiative heat transfer between graphene nanodisks. The strong plasmons supported by the nanodisks, as well as contributions from evanescent modes to the emission of these disks in the near-field, create a valuable platform to achieve rates of radiative transfer that exceed those of a blackbody. By taking advantage of this, combined with the active tunability of the plasmons supported by graphene nanostructures, we are able to achieve new, engineered heat transfer scenarios. To that end, by adjusting the Fermi level of nanodisks within an ensemble, we demonstrate the ability to send heat along a desired direction, thus enabling other, more complex behaviors, such as the heating of an arbitrary pattern of nanodisks, or even the isolation of a hot disk, which can store energy for long periods of time without releasing it until desired.

The results of our work serve as a foundation for the realization of a wide variety of technologies related to thermal management and energy harvesting. The active tunability of graphene, combined with its sharp and narrow spectral features, makes it an ideal platform to improve the efficiency of thermophotovoltaic devices, which have emerged as a promising platform to collect and use energy that would otherwise go to waste. Typically, the heat radiated to the environment by hot objects, such as engines, air conditioners, and factories, is largely wasted, since the majority of it is of much lower energy than the bandgap of the semiconductors used in solar cells; in this context, the goal of thermophotovoltaics is to absorb this heat and convert it to usable energy. In order for this to be possible, the device requires a component that can absorb thermal radiation in a broadband spectral range and reemit that energy in a narrow range matching the bandgap of the semiconductor.

Overall, our results form a new paradigm for manipulating the transfer of energy at the

nanoscale, and thus will serve to inspire the design and development of new devices requiring complete control over this process.

A Fluctuation-Dissipation Theorem

In order to average over the thermal fluctuations that appear in the derivation of the expression of the power absorbed by each nanodisk, we make use of the Fluctuation-Dissipation Theorem (FDT) [48, 49]. This relation connects the fluctuations of a physical quantity with the associated dissipation. For instance, for the case of the fluctuations of the dipole moment, the FDT takes the following form:

$$\langle p_i(\omega)p_j^*(\omega') \rangle = 4\pi\hbar\delta(\omega - \omega')\text{Im}\{\chi(\omega)\}\delta_{ij} \left[n(\omega, T) + \frac{1}{2} \right].$$

Here, i and j represent the components of the induced dipole, with $*$ being the complex conjugate. $\text{Im}\{\chi\} = \alpha_i(\omega) - (2i/3)k^3|\alpha_i(\omega)|^2$ to describe the absorption of the particles such that it satisfies the optical theorem even if they are nonabsorbing, and $n(\omega, T)$ the Bose-Einstein distribution. Similarly, for the fluctuations of the electric field \mathbf{E} , we have

$$\langle E_i(\mathbf{r}, \omega)E_j^*(\mathbf{r}', \omega') \rangle = 4\pi\hbar\delta(\omega - \omega')\text{Im}\{\delta_{ij}\mathbf{G}^0 + \mathbf{G}_{ij}(\mathbf{r}, \mathbf{r}', \omega)\} \left[n(\omega, T) + \frac{1}{2} \right],$$

with \mathbf{G}_{ij} being the dipole-dipole interaction tensor given in the main text by Equation (6) and \mathbf{G}^0 the radiation reaction term.

Acknowledgments

This work has been sponsored by the U.S. National Science Foundation (Grant ECCS-1710697). I acknowledge the UNM Center for Advanced Research Computing for the high-performance computing resources used in this work, and am also grateful for financial support from the Rayburn Reaching Up Fund, the New Mexico Space Grant Consortium, and the Barry Goldwater Scholarship and Excellence in Education Foundation.

I am also extremely thankful for the support that I have received from Alejandro, not only during the completion of this work, but throughout my undergraduate career. There is no question that I would not be the person that I am today if he had not taken a chance on me as a freshman. I can't thank him enough for the countless hours he has spent teaching me how to be a better researcher, scientist, and person, nor the endless patience he has shown for me throughout the last four years. His guidance and example have helped to shape my career aspirations and future goals.

Thank you also to Keith and Paul, who have made my time in the Theoretical Nanophotonics group exciting, for their support over the years, and for their enjoyable discussions in physics and beyond. Both of them set an example for me of the person I aspire to be.

Lastly, I am grateful to my parents, and to Jean Grasse, for instilling in me the work ethic that has made possible the completion of this thesis.

References

- [1] Naval Research and Development Framework <http://www.onr.navy.mil/en/our-research/naval-research-framework>.
- [2] Air Force Office of Scientific Research Broad Agency Announcement <http://afrl.dodlive.mil/funding/>.
- [3] NASA Technology Roadmaps. TA 14: Thermal Management Systems <http://www.nasa.gov/offices/oct/home/roadmaps/index.html>.
- [4] B. Guha, C. R. Otey, C. B. Poitras, S. Fan, , and M. Lipson, “Near-field radiative cooling of nanostructures,” *Nano Lett.*, vol. 12, pp. 4546–4550, 2012.
- [5] G. Brucoli, P. Bouchon, R. Haïdar, M. Besbes, H. Benisty, and J.-J. Greffet, “High efficiency quasi-monochromatic infrared emitter,” *Appl. Phys. Lett.*, vol. 104, p. 081101, 2014.
- [6] C. M. Hargreaves, “Anomalous radiative transfer between closely-spaced bodies,” *Phys. Lett.*, vol. 30A, pp. 491–492, 1969.
- [7] G. A. Domoto, R. F. Boehm, and C. L. Tien, “Experimental investigation of radiative transfer between metallic surfaces at cryogenic temperatures,” *J. Heat Transfer*, vol. 92, pp. 412–416, 1970.
- [8] D. Polder and M. Van Hove, “Theory of radiative heat transfer between closely spaced bodies,” *Phys. Rev. B*, vol. 4, pp. 3303–3314, 1971.
- [9] A. Manjavacas and F. J. García de Abajo, “Radiative heat transfer between neighboring particles,” *Phys. Rev. B*, vol. 86, p. 075466, 2012.
- [10] A. Manjavacas, S. Thongrattanasiri, J. J. Greffet, and F. J. García de Abajo, “Graphene optical-to-thermal converter,” *Appl. Phys. Lett.*, vol. 105, p. 211102, 2014.
- [11] L. Novotny and B. Hecht, *Principles of Nano-Optics*. New York: Cambridge University Press, 2006.
- [12] H. Xu, E. J. Bjerneld, M. Käll, and L. Börjesson, “Spectroscopy of single hemoglobin molecules by surface enhanced raman scattering,” *Phys. Rev. Lett.*, vol. 83, pp. 4357–4360, 1999.
- [13] J. N. Anker, W. P. Hall, O. Lyandres, N. C. Shah, J. Zhao, and R. P. Van Duyne, “Biosensing with plasmonic nanosensors,” *Nat. Mater.*, vol. 7, no. 6, pp. 442–453, 2008.
- [14] J. Olson, A. Manjavacas, L. Liu, W.-S. Chang, B. Foerster, N. S. King, M. W. Knight, P. Nordlander, N. J. Halas, and S. Link, “Vivid, full-color aluminum plasmonic pixels,” *Proc. Natl. Acad. Sci.*, vol. 111, pp. 14348–14353, 2014.
- [15] J. Olson, A. Manjavacas, T. Basu, D. Huang, A. E. Schlather, B. Zheng, N. J. Halas, P. Nordlander, and S. Link, “High chromaticity aluminum plasmonic pixels for active liquid crystal displays,” *ACS Nano*, vol. 10, pp. 1108–1117, 2016.

- [16] K. R. Catchpole and A. Polman, “Plasmonic solar cells,” *Opt. Express*, vol. 16, pp. 21793–21800, 2008.
- [17] H. A. Atwater and A. Polman, “Plasmonics for improved photovoltaic devices,” *Nat. Mater.*, vol. 9, pp. 205–213, 2010.
- [18] S. A. Maier, *Plasmonics: Fundamentals and Applications*. New York: Springer, 2007.
- [19] N. J. Halas, S. Lal, W. Chang, S. Link, and P. Nordlander, “Plasmons in strongly coupled metallic nanostructures,” *Chem. Rev.*, vol. 111, no. 6, pp. 3913–3961, 2011.
- [20] F. J. García de Abajo and A. Howie, “Relativistic electron energy loss and electron-induced photon emission in inhomogeneous dielectrics,” *Phys. Rev. Lett.*, vol. 80, pp. 5180–5183, 1998.
- [21] F. J. García de Abajo and A. Howie, “Retarded field calculation of electron energy loss in inhomogeneous dielectrics,” *Phys. Rev. B*, vol. 65, p. 115418, 2002.
- [22] P. B. Johnson and R. W. Christy, “Optical constants of the noble metals,” *Phys. Rev. B*, vol. 6, pp. 4370–4379, 1972.
- [23] F. H. L. Koppens, D. E. Chang, and F. J. García de Abajo, “Graphene plasmonics: A platform for strong light-matter interactions,” *Nano Lett.*, vol. 11, pp. 3370–3377, 2011.
- [24] A. N. Grigorenko, M. Polini, and K. S. Novoselov, “Graphene plasmonics,” *Nat. Photon.*, vol. 6, pp. 749–758, 2012.
- [25] J. Chen, M. Badioli, P. Alonso-González, S. Thongrattanasiri, F. Huth, J. Osmond, M. Spasenović, A. Centeno, A. Pesquera, P. Godignon, A. Zurutuza Elorza, N. Camara, F. J. García de Abajo, R. Hillenbrand, and F. H. L. Koppens, “Optical nano-imaging of gate-tunable graphene plasmons,” *Nature*, vol. 487, pp. 77–81, 2012.
- [26] Z. Fei, A. S. Rodin, G. O. Andreev, W. Bao, A. S. McLeod, M. Wagner, L. M. Zhang, Z. Zhao, M. Thiemens, G. Dominguez, M. M. Fogler, A. H. C. Neto, C. N. Lau, F. Keilmann, and D. N. Basov, “Gate-tuning of graphene plasmons revealed by infrared nano-imaging,” *Nature*, vol. 487, pp. 82–85, 2012.
- [27] H. Yan, X. Li, B. Chandra, G. Tulevski, Y. Wu, M. Freitag, W. Zhu, P. Avouris, and F. Xia, “Tunable infrared plasmonic devices using graphene/insulator stacks,” *Nat. Nanotechnol.*, vol. 7, pp. 330–334, 2012.
- [28] V. W. Brar, M. S. Jang, M. Sherrott, J. J. Lopez, and H. A. Atwater, “Highly confined tunable mid-infrared plasmonics in graphene nanoresonators,” *Nano Lett.*, vol. 13, pp. 2541–2547, 2013.
- [29] D. Rodrigo, O. Limaj, D. Janner, D. Etezadi, F. J. García de Abajo, V. Pruneri, and H. Altug, “Mid-infrared plasmonic biosensing with graphene,” *Science*, vol. 349, pp. 165–168, 2015.

- [30] L. Zundel and A. Manjavacas, “Spatially resolved optical sensing using graphene nanodisk arrays,” *ACS Photonics*, vol. 4, no. 7, pp. 1831–1838, 2017.
- [31] F. J. García de Abajo, “Graphene plasmonics: Challenges and opportunities,” *ACS Photon.*, vol. 1, pp. 135–152, 2014.
- [32] F. J. García de Abajo, “Multiple excitation of confined graphene plasmons by single free electrons,” *ACS Nano*, vol. 7, pp. 11409–11419, 2013.
- [33] I. Silveiro, J. M. Plaza Ortega, and F. J. García de Abajo, “Plasmon wave function of graphene nanoribbons,” *New J. Phys.*, vol. 17, p. 083013, 2015.
- [34] R. Yu, A. Manjavacas, and F. J. García de Abajo, “Ultrafast radiative heat transfer,” *Nat. Commun.*, vol. 8, p. 2, 2017.
- [35] A. Manjavacas, P. Nordlander, and F. J. García de Abajo, “Plasmon blockade in nanostructured graphene,” *ACS Nano*, vol. 6, pp. 1724–1731, 2012.
- [36] K. I. Bolotin, K. J. Sikes, Z. Jiang, M. Klima, G. Fudenberg, J. Hone, P. Kim, and H. L. Stormer, “Ultrahigh electron mobility in suspended graphene,” *Sol. State Commun.*, vol. 146, pp. 351–355, 2008.
- [37] C. R. Dean, A. F. Young, I. Meric, C. Lee, L. Wang, S. Sorgenfrei, K. Watanabe, T. Taniguchi, P. Kim, K. L. Shepard, and J. Hone, “Boron nitride substrates for high-quality graphene electronics,” *Nat. Nanotechnol.*, vol. 5, pp. 722–726, 2010.
- [38] L. Banszerus, M. Schmitz, S. Engels, J. Dauber, M. Oellers, F. Haupt, K. Watanabe, T. Taniguchi, B. Beschoten, and C. Stampfer, “Ultrahigh-mobility graphene devices from chemical vapor deposition on reusable copper,” *Sci. Adv.*, vol. 1, no. 6, 2015.
- [39] F. V. Ramirez and A. J. H. McGaughey, “Plasmonic thermal transport in graphene nanodisk waveguides,” *Phys. Rev. B*, vol. 96, p. 165428, 2017.
- [40] F. V. Ramirez, S. Shen, and A. J. H. McGaughey, “Near-field radiative heat transfer in graphene plasmonic nanodisk dimers,” *Phys. Rev. B*, vol. 96, p. 165427, 2017.
- [41] O. Ilic, N. H. Thomas, T. Christensen, M. C. Sherrott, M. Soljačić, A. J. Minnich, O. D. Miller, and H. A. Atwater, “Active radiative thermal switching with graphene plasmon resonators,” *ACS Nano*, vol. 12, no. 3, pp. 2474–2481, 2018.
- [42] L. Zhao, K. L. Kelly, and G. C. Schatz, “The extinction spectra of silver nanoparticle arrays: influence of array structure on plasmon resonance wavelength and width,” *J. Phys. Chem. B*, vol. 107, no. 30, pp. 7343–7350, 2003.
- [43] F. J. García de Abajo, “Colloquium: Light scattering by particle and hole arrays,” *Rev. Mod. Phys.*, vol. 79, pp. 1267–1290, 2007.
- [44] T. V. Teperik and A. Degiron, “Design strategies to tailor the narrow plasmon-photonic resonances in arrays of metallic nanoparticles,” *Phys. Rev. B*, vol. 86, p. 245425, 2012.

- [45] S. Baur, S. Sanders, and A. Manjavacas, “Hybridization of lattice resonances,” *ACS Nano*, vol. 12, pp. 1618–1629, 2018.
- [46] M. Nikbakht, “Radiative heat transfer in anisotropic many-body systems: Tuning and enhancement,” *J. Appl. Phys.*, vol. 116, no. 9, p. 094307, 2014.
- [47] E. Pop, V. Varshney, and A. K. Roy, “Thermal properties of graphene: Fundamentals and applications,” *MRS Bulletin*, vol. 37, pp. 1273–1281, 2012.
- [48] S. M. Rytov, *Theory of Electric Fluctuations and Thermal Radiation*. Bedford, MA: Air Force Cambridge Research Center, 1959.
- [49] A. Manjavacas and F. J. García de Abajo, “Vacuum friction in rotating particles,” *Phys. Rev. Lett.*, vol. 105, p. 113601, 2010.